Magmatic flare-up causes crustal thickening at the transition from subduction to continental collision

Carlos E. Ganade, Pierre Lanari, Daniela Rubatto, Joerg Hermann, Roberto F. Weinberg, Miguel A. S. Basei, Lucas R. Tesser, Renaud Caby, Yao Agbossoumondé, Caroline M. Ribeiro

communications earth & environment

ARTICLE

https://doi.org/10.1038/s43247-021-00103-z OPEN

Magmatic flare-up causes crustal thickening at the transition from subduction to continental collision

Carlos E. Ganade[1,2,3✉], Pierre Lanari[2], Daniela Rubatto[2,3], Joerg Hermann[2,3], Roberto F. Weinberg[4], Miguel A. S. Basei[5], Lucas R. Tesser[5], Renaud Caby[6], Yao Agbossoumondé[7] & Caroline M. Ribeiro[1,8]

Above subduction zones, magma production rate and crustal generation can increase by an order of magnitude during narrow time intervals known as magmatic flare-ups. However, the consequences of these events in the deep arc environment remain poorly understood. Here we use petrological and in-situ zircon dating techniques to investigate the root of a continental arc within the collisional West Gondwana Orogen that is now exposed in the Kabyé Massif, Togo. We show that gabbros intruded 670 million years ago at 20–25 km depth were transformed to eclogites by 620 million years ago at 65–70 km depth. This was coeval with extensive magmatism at 20–40 km depth, indicative of a flare-up event which peaked just prior to the subduction of the continental margin. We propose that increased H_2O flux from subduction of serpentinized mantle in the hyper-extended margin of the approaching continent was responsible for the increased magma productivity and crustal thickening.

[1] Geological Survey of Brazil/CEDES, Rio de Janeiro, Brazil. [2] Institut für Geologie, Universität Bern, Bern, Switzerland. [3] Research School of Earth Sciences, Australian National University, Canberra, Australia. [4] School of Earth, Atmosphere & Environment, Monash University, Clayton, Australia. [5] Instituto de Geociências, Universidade de São Paulo, São Paulo, Brazil. [6] Géosciences Montpellier, Université de Montpellier II, Montpellier CEDEX 5, France. [7] Université de Lomé, Lomé, Togo. [8] Universidade Federal do Rio de Janeiro, Rio de Janeiro, Brazil. ✉email: carlos.ganade@cprm.gov.br

Continental arcs are produced by subduction magmatism[1]. Determining their internal dynamics is a key to understanding the formation of continental crust[2]. At mid to deep crustal levels, continental arcs comprise dominantly magmatic additions from the mantle, pre-existing metasedimentary rocks, and various basement rocks of the upper plate[1]. Exposed tilted arc sections offer a unique opportunity to understand the deeper arc environment, such as those of the Salinian arc[3] and Famatinian arc[4], which expose 5–30 km of the arc crustal column. Deeper sections, such as the Fiordland arc[5,6] of New Zealand (15–55 km), show a gradual transition from shallower plagioclase-bearing igneous cumulates and granulite facies rocks to plagioclase-free, garnet-rich rocks (i.e., garnet-pyroxenites) and to eclogites[7].

Although there is a consensus that lower arc garnet-pyroxenite and eclogite protoliths are derived from mantle magma additions to arcs[1,8], there remains considerable controversy about the mechanism of formation of these plagioclase-free, garnet-rich lithologies. Their formation has implications for the origin of magmas in convergent plate margins. The most accepted models for the origin of garnet-pyroxenites in arc roots argue either that they represent high-pressure cumulates from a mantle-derived hydrous basalt or basaltic andesite, or that they are partial melting residues (restites) reflecting high pressure crystal–liquid equilibria at lower arc levels[1,8–10]. On the other hand, documentation from deep exposure of the Kohistan paleo-island arc (Northern Pakistan) is consistent with the formation of the lower arc garnet granulite by dehydration-melting of upper arc hornblende gabbronorite leading to intra-crustal differentiation and arc thickening to 30 km[11].

Crustal thickening to more than 50 km in Andean-type arcs is caused by complex processes that are as yet poorly-understood and involve a combination of tectonic shortening and magmatic accretion[12]. Igneous inflation has been postulated based on petrological investigation to explain arc thickening in other continental arcs such as in the Coast Plutonic Complex and Sierra Nevada of North America[13,14], Fiordland of New Zealand[15], and also in the Kohistan arc[11] in Pakistan.

Rates of magma addition in continental arcs are temporally discontinuous and characterized by short flare-ups, lasting 5–35 million years[16–18], and during which magma addition rates are up to fifteen times higher than background rates[17]. Ignition of flare-ups in arcs is an unresolved question with explanations ranging from upper plate crustal processes driven by internal arc feedback[19], to episodic mantle melting[4,18] and dynamic processes involving lithospheric thickening and delamination[20]. Flare-ups have so far been documented in upper crustal sequences, using the abundance of igneous rocks and their ages, detrital zircon ages of sedimentary rocks derived from the arc, and volume estimates of plutonic and volcanic rocks[17,21]. There has not yet been a detailed documentation of the consequences of these events to the deeper portion of the arcs. Although deep arc xenoliths offer important perspectives and their investigation has generated P-T paths, geochronology data, and even cooling rates[16], they return only random and punctuated information compared to exposed continental arc sections.

Here, we use petrochronology and thermodynamic simulations of lithologies from three different levels of the Kabyé Massif arc exposed in Togo, to show that deep parts of the arc were being pushed down into high pressure regions and internally reworked, while voluminous magma was being emplaced in the upper parts of the arc during a flare-up. Thus, we report for the first time the record and consequences of the flare-up phenomenon in deeper arc portions, responsible for doubling crustal thickness.

Sampling deep continental arc crust. The magmatic rocks of the continental arc system of the West Gondwana Orogen[22] intruded the old continental rocks of the Benino-Nigerian shield which extend to NE Brazil. This shield and its arc formed the overriding plate during continental collision with the West African Craton[23]. The Kabyé lower arc section is now preserved along the collisional suture zone and was exhumed to the surface by west-verging thrusts, along with ultra-high pressure eclogites, during the subduction of the West African craton margin[23–25] (Fig. 1A).

Shallower plutonic equivalents of the Kabyé lower arc section can be found in other sections of the West Gondwana Orogen, such as the Santa Quitéria plutonic arc complex in NE Brazil[26], and in its continuation in northwest Africa[23] (Fig. 1A). This arc system started as early as 880–800 Ma with juvenile magmatic additions, and culminated with voluminous batholith growth during the mature arc stage at 660–620 Ma[26]. Regardless of the arc level, the mafic rocks of the Kabyé Massif display positive εNd values at 600 Ma, ranging between 0 and +9 and low $^{87}Sr/^{86}Sr$ ratios from 0.7015 to 0.7051[24]. However, age-correlated felsic granitoids from the shallower mature stage of the Santa Quitéria arc, display increasingly negative εNd values and higher $^{87}Sr/^{86}Sr$ towards younger ages from 650 to 610 Ma[26]. Such dispersion of isotopic values has been interpreted as progressive contamination of juvenile magmas by a continental upper plate[26], as the arc thickened from 660 to 610 Ma. Together with regional geochronology of the shallower arc-related granitoids from NE Brazil and Togo[23,24,27], mature continental arc activity started at 660–640 Ma and finished with the final West Africa Craton passive margin subduction at c. 610 Ma[21].

The root of the Kabyé arc was formed by mantle-derived magmas[24,25] and now has a layered structure and comprises essentially deep meta-igneous and igneous rocks, that are exposed in a tectonically segmented monoclinal framework dipping 35–45° to the east[24,25] (Fig. 1B). Despite the several west-verging thrusts that crosscut it, disrupting the stratigraphic arc column, the massif still preserves an excellent semi-continuous exposure of the lower to middle arc section with primary igneous layering[24,25] (Fig. 1C). The trace element systematics of the rocks is in agreement with a continental arc setting[24]. Metamorphism and rock composition vary systematically across the massif. Garnet-pyroxenite lenses within strongly foliated garnet granulite dominate the western lower unit (the arc root) and grade into garnet-free metamorphosed pyroxenites, norites and diorites crosscut by kyanite-garnet-bearing felsic dykelets. The mafic granulites, originally metagabbros, from the lower unit are composed of garnet-clinopyroxene-plagioclase ± orthopyroxene with subordinate rutile and quartz, where garnet overgrows clinopyroxene indicating increasing pressure conditions[25]. These lower arc rocks are often migmatitic with residual garnet-pyroxenite accompanied by quartz-rutile-zoisite ± kyanite and retrogressive amphibole in association with plagioclase-rich leucosomes. The middle unit is composed of garnet-free orthopyroxene-clinopyroxene-plagioclase ± rutile ± quartz granulites and minor garnet-bearing granulites and garnet-free clinopyroxenites[24,25]. Finally, in the upper unit, xenoliths of garnet-bearing metagabbros occur within garnet-free metagabbros, which in turn have a conspicuous primary compositional igneous layering overprinted by a concordant metamorphic foliation[24].

We selected four samples from three different crustal levels of the tilted Kabyé continental arc for integrated petrology and geochronological investigation (see Detailed petrography and thin-section mapping in Supplementary items). Samples DKE-374 and DKE-371 are both anatectic high-pressure mafic rocks from the lower arc zone: DKE-374 represents the residual high-pressure eclogitic assemblage of garnet and clinopyroxene (Fig. 1B) while DKE-371 is a garnet-bearing, plagioclase-rich leucosome (Fig. 1C). Additionally, sample DKE-375 is a foliated

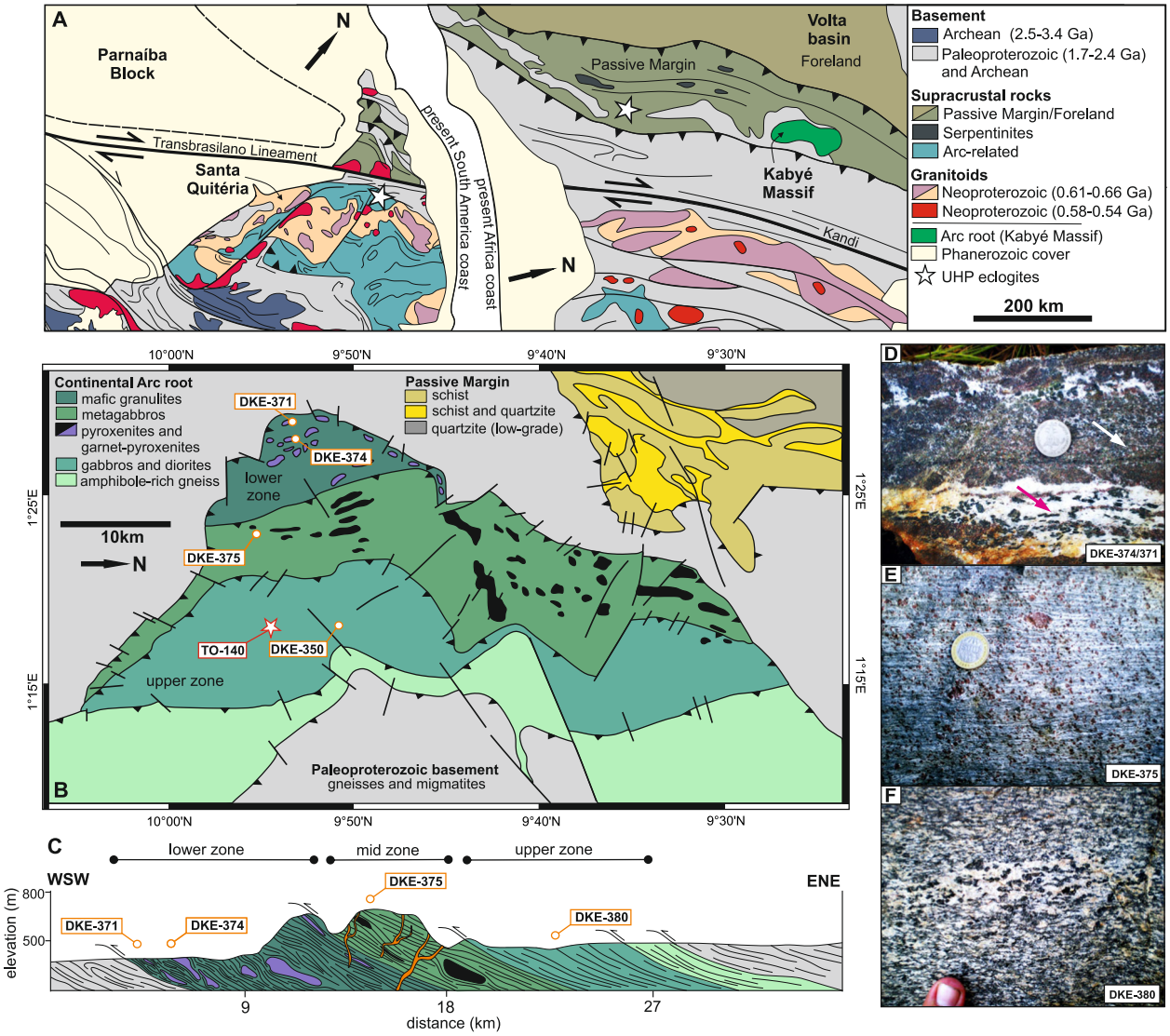

Fig. 1 Trans-Atlantic geological correlations and the Kabyé continental arc root. A Correlation between the geology of South America and Africa along the West Gondwana Orogen illustrating the location of the deep arc root of the Kabyé Massif and upper batholith zone of the Santa Quitéria arc exposed in NE Brazil. **B** Geological map of the Kabyé Massif based on ref. [70]. **C** Simplified cross section through the tilted arc crustal section of the Kabyé Massif showing the transition from garnet-bearing rocks on the left (west) to garnet-free metagabbros on the right (east). Late peraluminous felsic dikes are represented in orange. **D** Anatectic garnet-pyroxenite from the lower arc zone. White and pink arrows represent the residual eclogite sample (DKE-374) and the leucosome-rich sample (DKE-371), respectively. **E** Garnet granulite from the mid-arc zone (DKE-375). **F** Quartz-diorite from the upper arc (DKE-380).

garnet granulite from the middle-arc zone and sample DKE-380 is a weakly foliated quartz-diorite associated with garnet-free metagabbros of the upper arc zone.

Results: pressure–temperature (*P–T*) conditions and zircon geochronology. Thin sections of all garnet-bearing samples were compositionally mapped with EPMA to determine the chemistry zoning of minerals, and to derive the local bulk composition for forward and iterative *P–T* modeling. Figure 2 illustrates the approach taken for the most interesting garnet-pyroxenite sample (DKE-374). For samples DKE-371 and DKE-375 see Supplementary Fig. S1. The mineral assemblage map shows large idiomorphic garnets that are surrounded by interstitial pyroxene, amphibole, and quartz. Compositional maps show homogenous composition for the pyroxene with *X*Na (Na/(Na + Ca) = 0.26) and *X*Mg (Mg/(Mg + Fe) = 0.76) with a little rimward increase of the *X*Jd, thus classifying it as omphacite and the rock as an eclogite. Garnet is zoned with a more homogenous core with $Alm_{49\text{-}47}Py_{31\text{-}28}Grs_{25\text{-}18}Spe_{0.16\text{-}0.14}$ and a rim with $Alm_{46\text{-}42}Py_{27\text{-}21}Grs_{30\text{-}26}Spe_{0.13\text{-}0.09}$ (Fig. 2A).

Forward *P–T* modeling for this eclogite sample (DKE-374), using the local bulk composition of the mapped thin section, predicts the observed assemblage defining a *P–T* field between 1.60 and 2.25 GPa and 670–875 °C. The intersection of compositional isopleths of garnet and omphacite rims is between 1.86–2.10 GPa and 805–820 °C, yielding an average *P–T* condition of 815 ± 20 °C and 2.0 ± 0.2 GPa (Fig. 2B and Supplementary File Fig. S2). Our modeling indicates that amphibole is a retrograde phase. Iterative *P–T* modeling using the program Bingo–Antidote[28] integrated in XMapTools[29] defines a *P–T* region between 800 °C, 1.8 GPa and 900 °C, 2.5 GPa where there is a good match between observed assemblages and compositions, with optimal *P–T* conditions of 820 °C, 2.15 GPa (Fig. 2B and Supplementary File Fig. S3). Forward and iterative *P–T* modeling

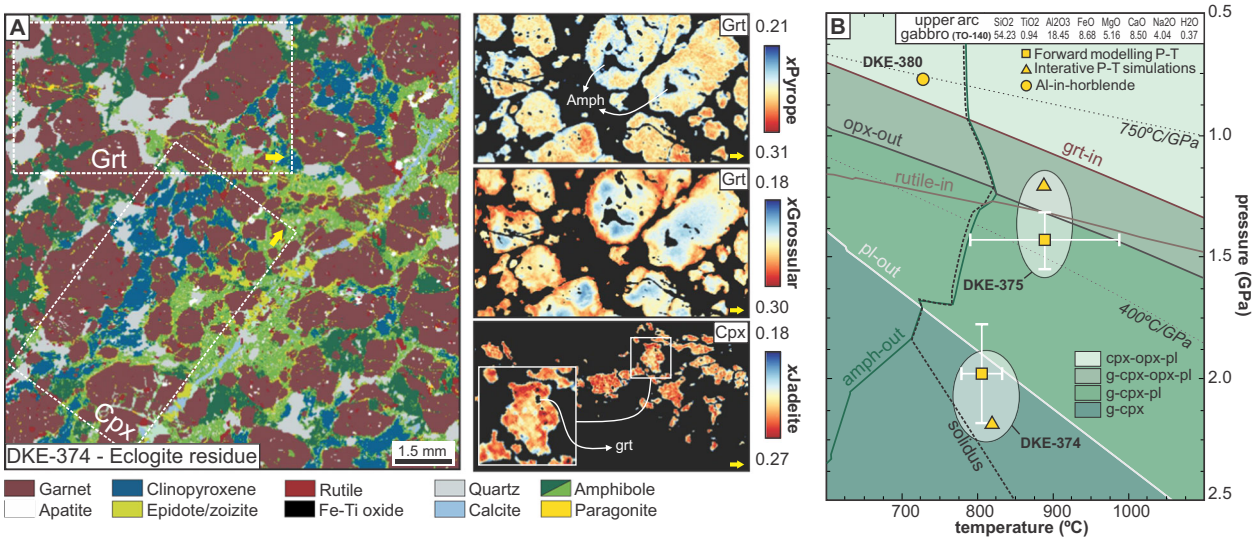

Fig. 2 Petrology of lower arc samples. A Mineral distribution of sample DKE-374. Compositional variation of garnet and clinopyroxene detailed within the dashed white boxes show rimward increase of the grossular component in garnet and subtle rimward increase of jadeite component in clinopyroxene. This sample is affected by post-peak fluid alteration along cracks responsible for the precipitation of calcite and a second stage of amphibole (light green). This late stage alteration was removed from the integrated pixel composition used in the forward and inverse modeling for P–T conditions. **B** P–T condition results for the samples from different arc levels. The background isochemical phase diagram, calculated using the composition of the upper arc, garnet-free metagabbro of sample TO-140 from ref. [3], shows different fields of mineral stability. Sample DKE-374 plots below the plagioclase-out field indicating eclogite facies conditions. Forward modeling *P–T* error bars are 95% of confidence level.

for the garnet-bearing metagabbro (sample DKE-375), show that the observed mineral assemblage and compositions are best modeled at conditions of 890 ± 100 °C and 1.4 ± 0.15 GPa and 890 °C and 1.2 GPa, respectively (Fig. 2B and Supplementary File Figs. S3 and S4). These conditions represent subsolidus equilibration after intrusion of the gabbro at $T > 1100$ °C. Starting from a garnet-free igneous gabbro intruded at 1.2–1.5 GPa, garnet is then formed during near-isobaric cooling[30]. Al-in-hornblende geobarometry[31] and plagioclase-hornblende geothermometry[32] for the diorite from the upper arc zone yield a narrow range of $P = 0.7 \pm 0.2$ GPa and $T = 720 \pm 20$ °C, also interpreted as isobaric cooling after emplacement.

Accordingly, the estimated pressure for the eclogite sample DKE-374 indicates a maximum depth of ~67 km (using 33.3 km GPa^{-1}, assuming a density of 3.0 g cm^{-3}). On the other hand, emplacement pressures of the upper section diorite of ~0.7 GPa are consistent with depths of 23 km, and of 1.18–1.44 GPa for the middle-section garnet metagabbro correspond to 39–48 km depth. These data indicate preservation of an arc section from 70 to 20 km, similar to that described in the Fiordland arc of New Zealand[6].

Zircon U-Pb ages coupled with trace element analysis for the lower arc eclogite (sample DKE-374) record a complex geological history, as revealed by zircon internal texture (Fig. 3A). Zircon imaging reveals core-rim structures in most zircon grains, together with minor homogenous and sector zoned grains. Trace element content and zircon internal texture indicate three different groups with progressive decrease of heavy rare earth elements (HREE), Y, Th/U and age. Weighted mean $^{206}Pb/^{238}U$ ages for these groups cluster at 671.6 ± 8.4, 634.5 ± 7.9, and 622.3 ± 6.8 Ma (all uncertainties provided are 95% confidence level) (Fig. 3A). For the oldest group with highest HREE and negative Eu, the c. 670 Ma age was calculated using the three oldest concordant analyses and is interpreted as the minimum age of the mafic protolith. Depletion in HREE together with the lack or attenuation of the negative Eu anomaly in the younger zircon groups (mostly rims and homogeneous grains) indicate that, in contrast to the older cores, they have grown in the presence of garnet and in the absence of plagioclase[33] (Fig. 3B). The complex patterns of zircon chemistry and texture are interpreted as recording first crystallization of the mafic protolith (high-HRRE group), at c. 670 Ma and progressive metamorphism with garnet growth and plagioclase breakdown marked by the two groups with mid-HREE to low-HREE zircon during arc development lasting until c. 620 Ma. The inset in Fig. 3C illustrates the combined decrease in Yb and negative Eu anomaly, indicating zircon growth during metamorphism with increasing garnet and decreasing plagioclase modal abundances for the garnet- and pyroxene-rich samples.

Zircon grains recovered from the plagioclase-rich leucosome (sample DKE-371) are rounded with sector zoning, typical of high-grade rocks[33]. Their very low U (2–15 ppm), Th/U (0.03–0.005) and trace element contents are comparable to the low-Yb group of sample DKE-374. The zircon Concordia age ($N = 11$) for this sample is 619.6 ± 9.8 Ma (2σ), which is within error of the age of the low-HREE metamorphic zircon rims in eclogite DKE-374 (Fig. 3B). The age is interpreted to date crystallization of the partial melt within the lower arc crust.

U-Pb ages and zircon trace element patterns for the shallower garnet metagabbro (sample DKE-375) and quartz-diorite (sample DKE-380) are less complex. Their zircons have oscillatory zoning and REE patterns of typical igneous grains[33]. The ages, therefore, constrain the crystallization of the protolith of the garnet metagabbro and quartz-diorite at 620.0 ± 5.9 and 623 ± 15 Ma, respectively (Supplementary File Fig. S5). This magmatic event is therefore contemporaneous with metamorphism in the lower unit as recorded by samples DKE-374 and DKE-371. The zircon REE pattern for DKE-375 indicates limited or no garnet growth during the crystallization of the magma, considering that zircon is a late crystallizing phase (Supplementary Fig. S5). Therefore, we interpret that in this sample garnet formed at subsolidus conditions during near-isobaric cooling at 1.2–1.4 GPa. While isobaric cooling can lead to minor garnet growth, it is impossible that it completely consumes plagioclase, which is indeed absent in

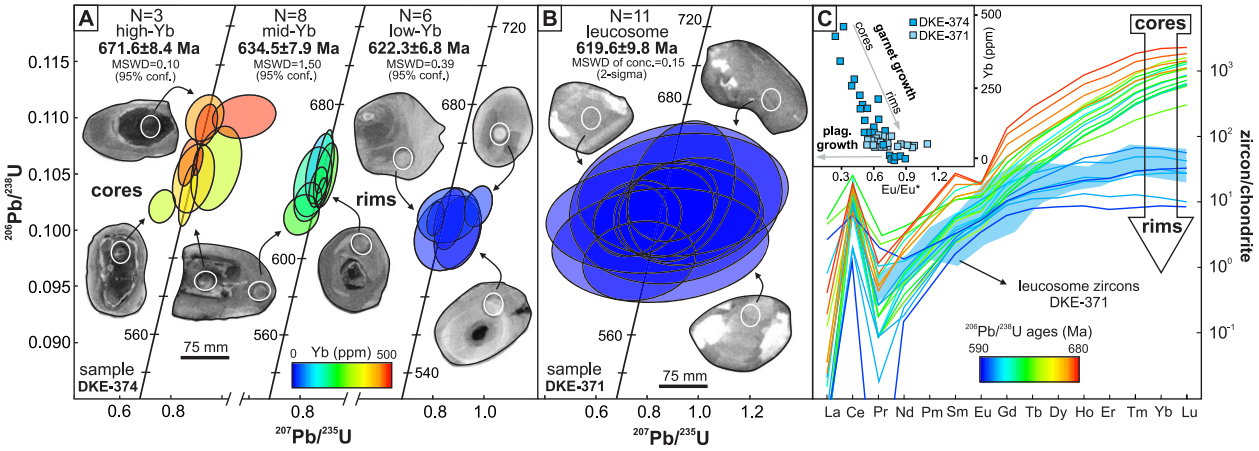

Fig. 3 Zircon geochronology and trace elements. Time-stamped zircon trace element variation for **A** Melt-poor residual eclogite (sample DKE-374) and **B** Plagioclase-rich leucosome (sample DKE-371) associated with the eclogitic residue. Reported ages for the sample DKE-374 are average $^{206}Pb/^{238}U$ ages. For the high-Yb group (zircon cores) the average $^{206}Pb/^{238}U$ ages for the oldest ($N = 3$) concordant zircons are considered the minimun age for the protolith. Age for the metamorphic zircon grains from leucosome of sample DKE-371 is a concordia age ($N = 11$). **C** Zircon trace element variation from zircon cores to rims as a function of $^{206}Pb/^{238}U$ ages for sample DKE-374. The light blue envelope represents zircon trace element for the leucosome-rich sample (DKE-371). Upper left inset illustrates the combined decrease in Yb and negative Eu anomaly, indicating zircon growth during metamorphism with increasing garnet modal abundance for samples DKE-374 and DKE-371.

sample DKE-374. The lack of plagioclase and presence of garnet provide additional evidence for burial and recrystallization of the gabbro at more than 60 km depth.

Discussion: arc thickening and igneous inflation. Time-stamped trace element patterns of zircon retrieved from the lower arc eclogite sample (DKE-374) indicate a minimum age for the protolith crystallization at c. 670 Ma outside of the stability field of garnet but within that of plagioclase. The lower arc bulk rocks have a pronounced positive Eu anomaly[24,25] that indicates plagioclase accumulation during formation of the layered igneous rocks (Fig. 4A). This demonstrates that the mafic protolith of the arc roots was initially a gabbro crystallized in the shallower arc, where plagioclase was stable. Progressive pressure increase recorded by HREE depletion in younger zircon domains and by the metamorphic mineral assemblage, suggests that the gabbro was buried to depths of ~67 km within the arc column, at peak pressure of ~2.0 GPa by c. 620 Ma. Moreover, prograde garnet and omphacite zoning and clinopyroxene coronas around garnet[24,25] similarly indicate increasing pressure conditions. The age of metamorphism in the eclogite (sample DKE-374) overlaps with crystallization ages of the magmatic protolith of the garnet granulite (DKE-375) and quartz diorite (DKE-380) in the middle to upper arc crust. This indicates that new mafic magmas did not stall at the crust-mantle boundary but rather intruded close to the neutral buoyancy zone at a depth of 23 km in the case of the upper quartz diorite, or crystallized at high-pressure conditions at depths of 39–48 km in the case of the garnet granulite.

It is suggested that the burial of gabbro from 23 to 67 km depths between 634 and 620 Ma is related to an inflation of the crust driven by an increased rate of magma emplacement at 20–25 km depth and subordinately at higher pressures, peaking at c. 620 Ma. This inferred increase in magmatism coincides with a pronounced peak at c. 620 Ma in the age distribution of detrital zircon from sediments in the basins and igneous zircons from granitoids related to the arc in Togo and NE Brazil[23,26,27,34,35] (Fig. 4B). The combined data suggest that this time period marks a magmatic flare-up coeval with the burial, metamorphism, and anatexis of earlier intrusions and formation of garnet–pyroxenites and eclogites in the deep part of the arc.

The flare-up event was active c.10 million years prior to the collision with the passive margin of the West African Craton, which is marked by ultra-high pressure (UHP) eclogites dated at c. 610 Ma[22]. During this 10 million years time interval, 500 km of lithosphere would have been subducted at average plate velocities of 5 cm year^{-1}. This distance is in accordance with the width of the hyper-extended modern Iberian passive margin, that exposes serpentinized sub-continental lithospheric mantle over a 170 km wide section[36]. One of the features of the preserved passive margin of the West African Craton is the abundance of serpentinized peridotites interpreted to mark a continental-ocean transition zone[37–39]. Subduction of these serpentinites and release of H_2O during antigorite and chlorite breakdown at 80–120 km depths can increase the H_2O flux to the subarc mantle by a factor of six compared to expected flux from breakdown of hydrous phases in altered oceanic crust[40,41]. This scenario is modeled in Fig. 5A where different lithospheric segments enter the subduction zone during transition from subduction to collision. Up to about 20 million years prior to collision, oceanic lithosphere is subducted where hydrous phases are concentrated in the mafic oceanic crust. This is followed by subduction of the ocean-continent transition zone that is dominated by serpentinites. Finally, the extended continental margin enters the subduction zone, leading to continental collision. The different water content of the subducted lithospheric segments controls partial melting of the subarc mantle, and hence magmatic addition to the upper arc environment. For the normal oceanic lithosphere water content (0.17×10^9 g of H_2O) is assumed to be stored in a 2 km-thick upper volcanic layer of altered basalts (lawsonite-eclogite, 1 wt% H_2O) and a 3 km-thick layer of peridotites with an average serpentinization of 10%. For the exhumed mantle in the hyperextended margin, the water content (1.07×10^9 g of H_2O) is stored in a 3 km-thick upper zone of fully serpentinized peridotite with a progressive decrease of serpentinization to 70, 40, 20, and 10% to 7 km[42] and assuming 9 wt% H_2O stored in the serpentinites at sub-arc depth[43]. In the calculations we use a vertical section with a unit area of 1 m^2, thus this number represents the quantity of water in a column of 1 m^2 at sub-arc P–T conditions. The response of the arc to the varying magma production driven by these varying H_2O inputs in the hot

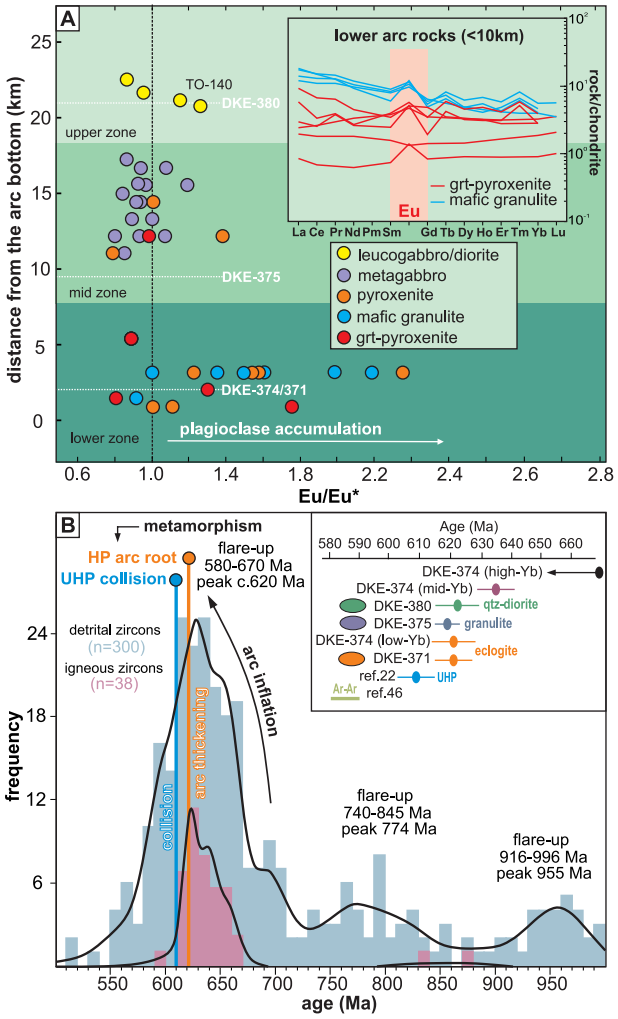

Fig. 4 Magmatic flare-up record from shallower arc rocks. A Distribution of Eu/Eu* anomalies from bulk-rock across the Kabyé arc root with respect to distance from the westernmost boundary of the massif (near sample DKE-371 in Fig. 1B), which represents the arc deepest position (proxy for arc depth). The samples from the arc bottom have predominantly positive Eu anomalies suggesting shallower crystallization/differentiation, within the plagioclase stability field. Inset shows REE distribution and the positive Eu anomaly of selected samples from the lower arc rocks. Data from ref. [24]. **B** Age distribution of detrital and igneous zircons from arc-related basins and granitoids from Togo and NE Brazil[23,26,27,34,35] depicting maximum magmatic addition rate at 620–625 Ma within a 660–580 flare-up. Inset: distribution of U-Pb and Ar-Ar[43] ages from the igneous and metamorphic rocks of the Kabyé arc root.

mantle wedge is illustrated in the lower panel of Fig. 5A. With time, the arc thickens with accumulation of mantle-derived magmas at the neutral buoyancy level, favored by subduction of water-rich, serpentinized mantle that ignites the flare-up at 630–620 Ma. The maximum arc thickness resulting from this process as constrained by our samples is ~70 km.

We suggest that this increased H_2O flux ignited the magmatic flare-up immediately preceding collision. In the Gangdese arc, in South Tibet, a similar flare-up immediately predating collision has also been recorded[44]. There, continental arc magmatism associated with the Tethyan oceanic lithosphere subduction lasted for c. 160 million years, until continental collision between India and Asia shut down the system, marked by the Kaghan and Tso Morari UHP eclogites dated at 50-45 Ma[44,45]. In this context, a similar flare-up event is evident 5–10 million years. before UHP metamorphism associated with subduction of the Indian passive margin[44]. The similar history in West Gondwana and Himalayan orogens suggests that geometry and composition of the transitional region between ocean and continents modulates the intensity of magmatism in the period immediately preceding continental collision.

Using thermodynamic simulations, we modeled the progressive transformation of an upper arc gabbro to an anatectic residual eclogite due to burial in response to magmatic inflation resulting from a flare-up. The mineral assemblage and modes observed in sample DKE-374 are modeled at 800–850 °C and 1.9–2.0 GPa using the upper arc gabbro composition TO-140 from ref. [3]. (Fig. 5B). Burial leads to an increase in density from 3.0 g cm^{-3} in the gabbro to up to 3.4 g cm^{-3} in the eclogite. As the ignition of the flare-up and thickening of the arc crust was immediately followed by subduction of the continental margin at 615–610 Ma[22] (Fig. 6A), we speculate that, despite the high density of the eclogites in the arc roots, there was not enough time for the instability to develop into delamination[7]. Moreover, the dragging down of buoyant incoming continental crust at the start of the collision provided a support and a natural barrier, that impeded eclogite delamination. The thickening of the arc was likely accompanied by compressive forces, as is common in other continental arcs[12], however the relative contributions of tectonic shortening and magma inflation to crustal thickening could not be estimated. Although the densification of the arc root could lead to the enhanced compression in the upper arc[7], there is still no clear indication that this process could also generate low pressure gradients in the arc column that would favor magmas to stall at the neutral buoyancy zone. During and after continental collision at c. 610 Ma[21], thrusting toward the west exposed the deep roots of the continental arc at 600–580 Ma[46]. Thrusting was coupled with dextral transcurrent tectonics along the suture zone, and was responsible for displacing the batholith-dominated zone to present-day NE Brazil[22] (Fig. 6B, C).

This is the first study that recognizes the impact of a magmatic flare-up on the roots of continental arcs. The flare-up combined with background compressive tectonic stresses led to a significant crustal thickening[12]. Thus, we conclude that magmatic flare-up causing inflation in arcs represents a new and alternative model to explain thick arc roots and the origin of garnet-pyroxenites and eclogites in their deep sections. Detailed P–T–time evolution of exhumed arc roots provides an important link between processes in the lower crust with those in upper crust. The results presented provide insights into the interplay of fast crustal growth and thickening in response to a magmatic flare-up at the termination of a long-lived subduction system.

Methods

Mineral chemistry and quantitative petrological maps. The samples were analyzed by electron probe micro-analyser (EPMA) using both quantitative spot analyses and X-ray compositional mapping in wavelength-dispersive mode. EPMA analyses were acquired with a JEOL JXA-8200 superprobe at the Institute of Geological Sciences (University of Bern and Federal University of Rio de Janeiro, the latter only for plagioclase and amphibole of sample DKE-380). Conditions for spot analyses were 15 keV accelerating voltage, 10 nA beam current and 40 s dwell times (including 2 × 10 s of background measurement). The following standards were used: almandine (Si, Fe, and Al), forsterite (Mg), orthoclase (K), anorthite (Ca), albite (Na), tephrite (Mn) and ilmenite (Ti) for garnet, and wollastonite (Si), orthoclase (K), anorthite (Al, Ca), albite (Na), forsterite (Mg), almandine (Fe), tephrite (Mn), and ilmenite (Ti) for pyroxene and amphibole. Compositional maps follow the procedure described in ref. [47] using 15 KeV accelerating voltage, 100 nA beam current and dwell times of 200 ms. Three maps of 1000 × 1000 pixels over areas of 15 × 15 mm^2 were acquired on samples DKE-374, DKE-371 and DKE-375 (Fig. 2 and Supplementary File Fig. S1). Point analyses were measured on the same area to be used as internal standards[48]. The compositional maps were classified and converted into concentration maps of oxide weight percentage using the software XMapTools 2.3.1[49] (Supplementary Data 1). Local bulk compositions (Supplementary File Fig. S3) were approximated from combined oxide weight percentage

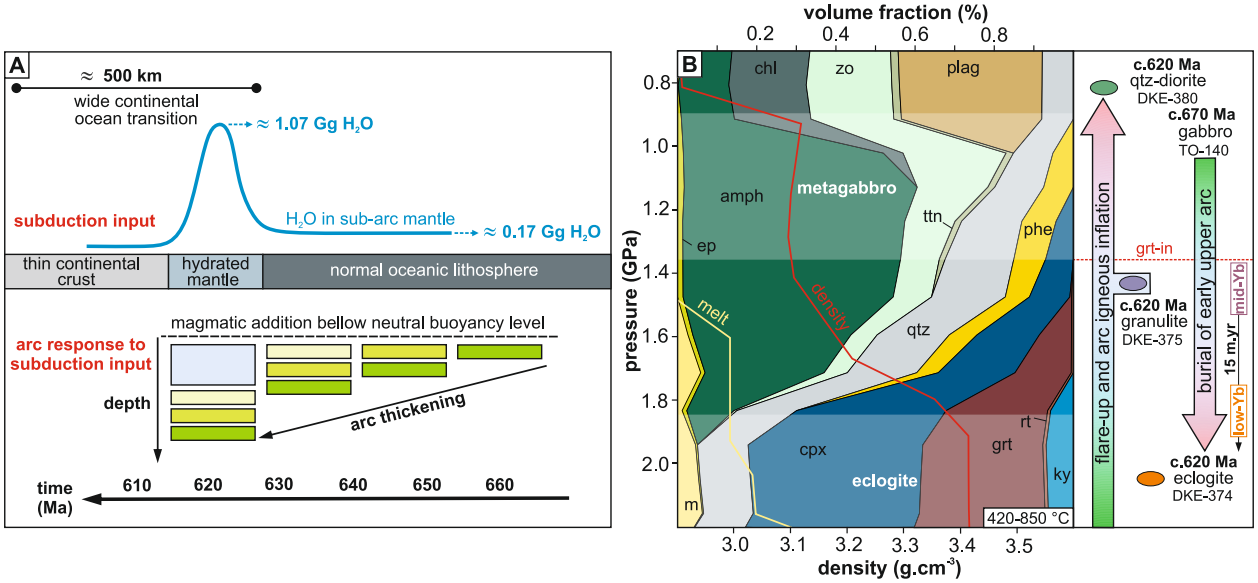

Fig. 5 Igneous inflation and arc thickening during different stages of subduction. A Upper panel: amount of water in the different sections of subducted crust in a column of 1 m^2 at sub-arc P–T conditions (see text for details). Lower panel: response of the arc to varying magma production, caused by varying H_2O release of the subducting slab over time. The different colors of the boxes (dark green to light blue) indicates arc crust produced at different time intervals (time scale at the bottom). **B** Change in modal abundance of residual phases during burial of an upper arc metagabbro (sample TO-140 from ref. [24].). Thick yellow line: extracted melt; thick red line: density variation of the residual phases. Mineral abbreviations: amph amphibole, chl chlorite, zo zoisite, ep epidote, ttn titanite, plag plagioclase, qtz quartz, cpx clinopyroxene, phe phengite, grt garnet, rt rutile, ky kyanite, and m melt. Left panel illustrates the process of flare-up and upper arc igneous inflation with coeval burial of earlier shallower arc to eclogitic conditions. The 15 millon years span from the garnet-in isograd to eclogitic conditions is constrained by the mid-Yb and low-Yb zircon rims of sample DKE-374.

maps using the export built-in function of XMapTools by integrating the pixel compositions of particular domains after a density correction[50,51].

Imaging of internal zoning. Zircons were separated from the crushed rock samples using usual heavy liquid and magnetic techniques. Grains were mounted in epoxy resin and polished down to expose the near-equatorial section. Imaging of zircon grains was acquired at the Research School of Earth Sciences (RSES), at the Australian National University, and at the Geochronological Research Center (CPGeo), at the University of São Paulo (USP). Cathodoluminescence (CL) imaging at RSES was done in a JEOL-6610A scanning electron microscope (SEM) supplied with a Robinson detector for cathodoluminescence. Operating conditions for the SEM were 15 kV, 70 mA and a 20 mm working distance. In São Paulo, CL images were obtained using a Quanta 250 FEG SEM prepared with a Centaurus Mono CL3 detector for cathodoluminescence.

Sensitive high-resolution ion micro probe. Zircon grains were analysed for U, Th, and Pb in the epoxy mount using the SHRIMP-II at the Research School of Earth Sciences (RSES) at the Australian National University (ANU) and the SHRIMP-IIe at the University of São Paulo. SHRIMP conditions and data acquisition were generally as described previously[52]. Each data point was collected in sets of six scans throughout the masses and a reference zircon (TEM2)[53] was analyzed each fourth analysis. Measured $^{207}Pb/^{206}Pb$ ratios (Supplementary Data 2) were used in common Pb corrections. The common Pb composition was assumed to be that predicted by the model of ref. [54]. U-Pb data were collected over three analytical sessions using the same standard, with the different sessions having calibration errors between 1.21% and 2.11% (2-sigma), which was propagated to single analyses. Data evaluation and age calculation were respectively performed in the softwares Squid and Isoplot/Ex[55,56]. Average $^{206}Pb/^{238}U$ ages are quoted at the 2-sigma and 95% confidence level.

Trace elements. Zircon trace elements (Supplementary Data 2) were analyzed by laser-ablation inductively coupled plasma mass spectrometry (LA-ICP-MS) at RSES. This instrument includes an ANU "HelEx" laser ablation cell[57] built to receive a pulsed 193 nm wavelength ArF Excimer laser with 100 mJ output energy at a repetition rate of 5 Hz and coupled to an Agilent 7500 quadrupole ICPMS. The instrument was tuned for maximum sensitivity and minimum production of molecular species, maintaining ThO+/Th+ at <0.5%. The laser was operated in drilling mode with spot sizes of 28 µm. Total analysis time was 60 s, where the first 25 s of which was background acquisition before ablation. Synthetic glasses (NIST 612 for zircon) were used for external calibration[58]. The SiO_2 value of 32.45 wt% was used for internal standard for zircon. A secondary natural glass standard (BCR-2) was used to monitor accuracy. Data reduction and evaluation was performed in the software package Iolite v.2.5 and then normalized with the chondrite[59] composition.

Forward thermodynamic modeling. Pseudosections (isochemical sections) were constructed using the THERIAK-DOMINO software[60] (version 04.02.2017) with the internally consistent thermodynamic data of ref. [61]. Modeling was performed using eight-components for sample DKE-375 in the system Na_2O-CaO-FeO-MgO-Al_2O_3-$SiO2$-TiO_2-O_2 and using nine-components for sample DKE-374 in the system Na_2O-CaO-FeO-MgO-Al_2O3-SiO_2-H_2O-TiO_2-O_2. K_2O and MnO were not considered in the models due to lack of mica, K-feldspar and negligible spessartine in garnet. The following solid solution models were used in pseudosection modeling: garnet, orthopyroxene, spinel and melt[62], ilmenite-hematite[63], amphibole[64], omphacite[65], feldspars[66], epidote, talc, and chlorite[60]. Pure phases included rutile, quartz, Al_2SiO_5 isomorphs and H_2O. The bulk compositions used were calculated from the compositional maps. The pseudosection of anhydrous DKE-375 sample was calculated in the *P*–*T* window of 0.5–2.0 GPa and 600–1100 °C, for equilibrium assemblage composed of garnet, clinopyroxene, plagioclase, quartz, rutile, and Fe-Ti oxides. For sample DKE-374, a P-MH_2O model was calculated to evaluate the effects of water in bulk composition at fixed temperature of 750 °C based on unpublished Zr-in-rutile thermometry. The amount of water varies from anhydrous conditions at the left-hand side (H_2O = 0.001 wt% normalized) to hydrated conditions (H_2O = 2.09 wt% normalized) at the right-hand side. The pseudosection of sample DKE-374 was calculated using MH_2O = 0.06 (equivalent to 0.13 wt% of H_2O normalized) in the *P*–*T* window of 1.0–2.5 GPa and 600–1100 °C, looking for metamorphic peak assemblage composed of garnet, omphacite, quartz, epidote, rutile, and melt. Tiny amount of extra oxygen (*O* = 0.001 mol) was added to the bulk composition of both samples in order to stabilize the ferric-bearing end-members of solid solution models. The peak *P*–*T* conditions were calculated using isopleth interception thermobarometry and the average results are reported at 95% of confidence level.

Forward thermodynamic simulation. A computer model ArcMod based on a dynamic evolution of the reactive bulk composition during prograde metamorphism was developed to simulate the solid-state transformation and melt production of a rock unit during burial and heating in continental arc settings. This model simulates for a set of *P*–*T* trajectories and for a variety of rock systems, the progressive changes in (1) mineral assemblages, (2) mineral and melt compositions, (3) melt and solid bulk chemistry, (4) rock density. The thermodynamic model relies on Gibbs energy minimizations performed using THERIAK[60], and the most up-to-date thermodynamic datasets and activity models for mafic rocks[67,68]. ArcMod includes three additional subroutines that can adjust the reactive bulk

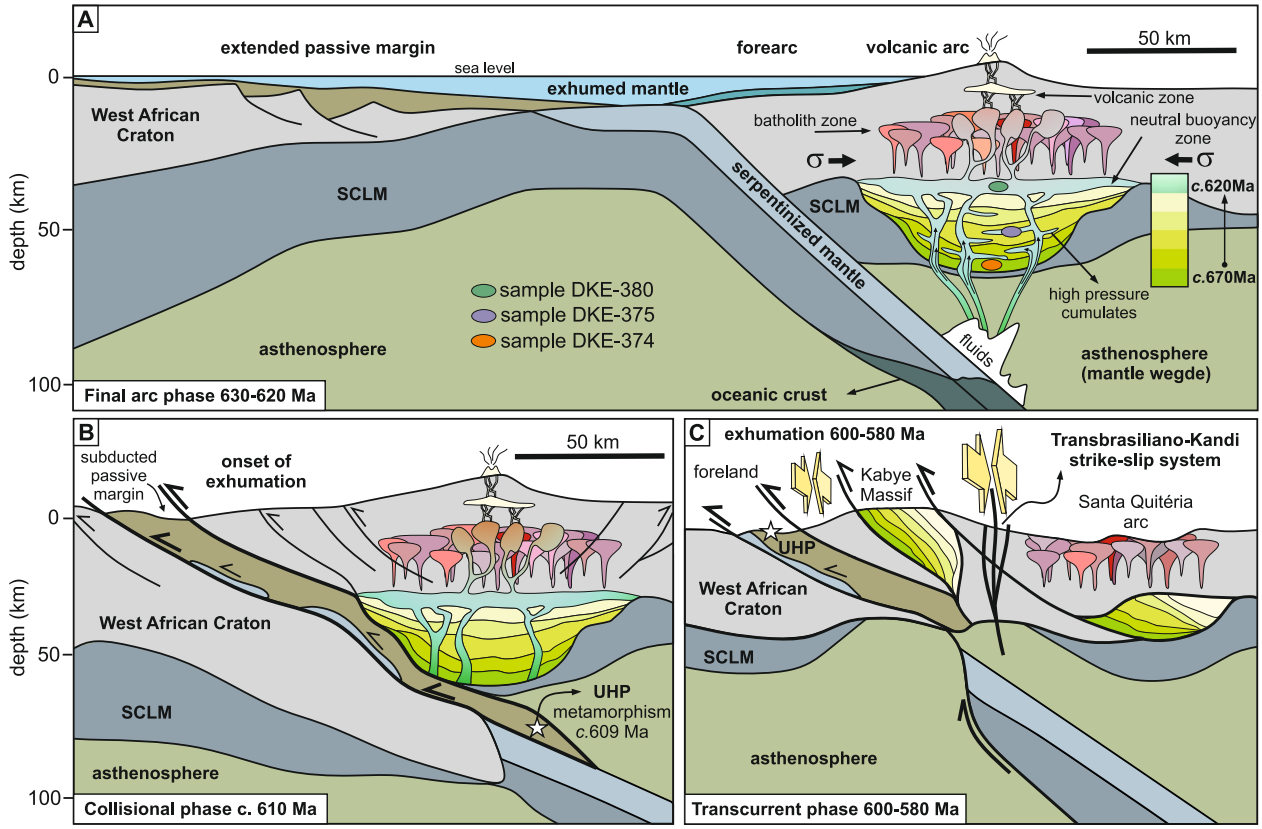

Fig. 6 Integrated model for arc thickening and preservation of arc root. A Continental arc building (650–620 Ma) through a series of sheeted intrusions. The lower portion of the arc pile, under background compressive tectonic stresses related to convergence and subduction, has been depressed by the emplacement of younger mantle-derived and shallower intrusions, leading to arc thickening and metamorphism of the once shallower gabbro intrusions. Small sills may be emplaced in the deeper levels of the arc originating high-P cumulatic and magmatic rocks, represented by our sample DKE-375. Magma differentiation to intermediate or felsic arc rocks may occur in several levels but predominantly in the neutral buoyancy zone, represented by the quartz-diorite sample DKE-380. Fluid release from serpentinized mantle triggered mantle melting and arc flare-up. **B** Continental collision at c. 610 Ma and subduction of the West African Craton and associated passive margin to depths of UHP metamorphism (>90 km), leading to onset of exhumation and upper plate uplift. **C** Exhumation (600–580 Ma) through thrust zones and exposure of deep arc roots of the Kabyé Massif. Continuous shortening due to Himalayan-type continental collision results in the formation of the major (>4000 km long) right-handed Transbrasiliano-Kandi strike-slip system.

composition at every step to maintain H_2O saturation at subsolidus condition, to simulate water-fluxed melting and/or melt extraction. Each bulk rock composition was treated as a separate system without any possible interaction between them. The numerical strategy is described in the following. Firstly, ArcMod computes the minimum H_2O content required for water saturation at the starting subsolidus conditions. This value is applied to maintain water saturation conditions with only 0.01 vol% excess water at the first iteration. Then, if a H_2O fluid phase is predicted to be stable at any step, the corresponding H_2O content is fractionated from the reactive bulk composition before performing the next iteration. This ensures that water saturation is maintained throughout the subsolidus space but without producing a pure H_2O phase above the permeability threshold of 0.01 vol%. Melt extraction occurs in the model when the melt fraction exceeded an arbitrary threshold fixed at 7 vol%. The rock is assumed to retain a fraction of 1 vol% of melt at the end of each extraction stage. A volume factor, representing the volume of the reactive system after H_2O and/or melt extraction, is approximated after each iteration[69]. The amount of H_2O in the melt was monitored and maintained above the threshold of 6 wt% in order to simulate water-fluxed melting. When required, the bulk H_2O was increased (by adding external H_2O fluid), to raise the amount of H_2O in the melt to the threshold value of 6 wt%. Note that water-fluxed melting is only predicted to occur at pressure above 2.2 GPa for the P–T trajectory shown in Fig. 5B. Results of ArcMod are presented as mod-box diagrams depicting the evolution of the volume fraction of solids, in addition to the total amount of silicate melt produced during prograde metamorphism.

Data availability

All data generated during the study, including in-situ zircon U-Pb combined with trace element and mineral EPMA analyses are available in supplementary information file (Supplementary Data 1 and 2). Bulk-geochemistry used in thermodynamic modeling in Figs. 2B and 5B as well as trace elements in Fig. 4A are available in ref. [24]. Age distribution of detrital and igneous zircons from arc-related basins and granitoids from Togo and NE Brazil in Fig. 4B are available in refs. [23,26,27,34,35]. The datasets generated during in this study are available in the Figshare repository (https://figshare.com/s/6e6f03024663ac213a7e and https://figshare.com/s/52c03f49895757ec249f).

Received: 29 July 2020; Accepted: 14 January 2021;
Published online: 22 February 2021

References

1. Ducea, M. N., Saleeby, J. B. & Bergantz, G. The architecture, chemistry, and evolution of continental magmatic arcs. *Annu. Rev. Earth Planet. Sci.* **43**, 299–331 (2015).
2. Hawkesworth, C. J. & Kemp, A. I. S. Evolution of the continental crust. *Nature* **443**, 811–817 (2006).
3. Kidder, S., Ducea, M., Gehrels, G., Patchett, P. J. & Vervoort, J. Tectonic and magmatic development of the Salinian Coast Ridge belt, California. *Tectonics* **22**, 45–56 (2003).
4. Otamendi, J. E., Ducea, M. N. & Bergantz, G. W. Geological, petrological and geochemical evidence for progressive construction of an arc crustal section, Sierra de Valle Fertil, Famatinian Arc, Argentina. *J. Petrol.* **53**, 761–800 (2012).
5. Clarke, G. L., Daczko, N. R. & Miescher, D. Identifying relic igneous garnet and clinopyroxene in eclogite and granulite, Breaksea Orthogneiss, New Zealand. *J. Petrol.* **55**, 1921–1938 (2013).
6. De Paoli, M. C., Clarke, G. L., Klepeis, K. A., Allibone, A. H. & Turnbull, I. M. The eclogite–granulite transition: Mafic and intermediate assemblages at Breaksea Sound, New Zealand. *J. Petrol.* **50**, 2307–2343 (2009).

7. Lee, C. T. A. & Anderson, D. L. Continental crust formation at arcs, the arclogite "delamination" cycle, and one origin for fertile melting anomalies in the mantle. *Sci. Bull.* **60**, 1141–1156 (2015).
8. Lee, C. T. A., Cheng, X. & Horodyskyj, U. The development and refinement of continental arcs by primary basaltic magmatism, garnet pyroxenite accumulation, basaltic recharge and delamination: insights from the Sierra Nevada, California. *Contrib. Mineral. Petrol.* **151**, 222–242 (2006).
9. Saleeby, J., Ducea, M. & Clemens-Knott, D. Production and loss of high-density batholithic root, southern Sierra Nevada, California. *Tectonics* **22**, 6 (2003).
10. Alonso-Perez, R., Müntener, O. & Ulmer, P. Igneous garnet and amphibole fractionation in the roots of island arcs: experimental constraints on andesitic liquids. *Contrib. Mineral. Petrol.* **157**, 541–558 (2009).
11. Garrido, C. J. et al. Petrogenesis of mafic garnet granulite in the lower crust of the Kohistan paleo-arc complex (northern Pakistan): implications for intra-crustal differentiation of island arcs and generation of continental crust. *J. Petrol.* **47**, 1873–1914 (2006).
12. Cao, W., Paterson, S., Saleeby, J. & Zalunardo, S. Bulk arc strain, crustal thickening, magma emplacement, and mass balances in the Mesozoic Sierra Nevada arc. *J. Struct. Geol.* **84**, 14–30 (2016).
13. Chin, E. J., Lee, C. T. A., Luffi, P. & Tice, M. Deep lithospheric thickening and refertilization beneath continental arcs: case study of the P, T and compositional evolution of peridotite xenoliths from the Sierra Nevada, California. *J. Petrol.* **53**, 477–511 (2012).
14. Brown, E. H. & Walker, N. W. A magma-loading model for Barrovian metamorphism in the southeast Coast Plutonic Complex, British Columbia and Washington. *Geol. Soc. Am. Bull.* **105**, 479–500 (1993).
15. Brown, E. H. High-pressure metamorphism caused by magma loading in Fiordland, New Zealand. *J. Metamorph. Geol.* **14**, 441–452 (1996).
16. Chin, E. J., Lee, C.-T. A. & Blichert-Toft, J. Growth of upper plate lithosphere controls tempo of arc magmatism: constraints from Al-diffusion kinetics and coupled Lu-Hf and Sm-Nd chronology. *Geochem. Perspect. Lett.* **1**, 20–32 (2015).
17. Paterson, S. R. & Ducea, M. N. Arc magmatic tempos: gathering the evidence. *Elements* **11**, 91–98 (2015).
18. Ardila, A. M. M., Paterson, S. R., Memeti, V., Parada, M. A. & Molina, P. G. Mantle driven cretaceous flare-ups in Cordilleran arcs. *Lithos* **326**, 19–27 (2019).
19. Ducea, M. N. The California arc: thick granitic batholiths, eclogitic residues, lithospheric-scale thrusting, and magmatic flare-ups. *GSA Today* **11**, 4–10 (2001).
20. DeCelles, P. G., Ducea, M. N., Kapp, P. & Zandt, G. Cyclicity in Cordilleran orogenic systems. *Nat. Geosci.* **2**, 251–257 (2009).
21. De Silva, S. L., Riggs, N. R. & Barth, A. P. Quickening the pulse: fractal tempos in continental arc magmatism. *Elements* **11**, 113–118 (2015).
22. Ganade de Araujo, C. E. G. et al. Ediacaran 2500-km-long synchronous deep continental subduction in the West Gondwana Orogen. *Nat. Commun.* **5**, 5198 (2014).
23. Ganade, C. E. et al. Tightening-up NE Brazil and NW Africa connections: advances in zircon geochronology towards a complete plate tectonic cycle in the Dahomeyide belt of the West Gondwana Orogen in Togo and Benin. *Precambrian Res.* **276**, 29–42 (2016).
24. Duclaux, G., Ménot, R. P., Guillot, S., Agbossoumondé, Y. & Hilairet, N. The mafic layered complex of the Kabyé massif (north Togo and north Benin): Evidence of a Pan-African granulitic continental arc root. *Precambrian Res.* **151**, 101–118 (2006).
25. Guillot, S. et al. Transition from subduction to collision recorded in the Pan-African arc complexes (Mali to Ghana). *Precambrian Res.* **320**, 261–280 (2019).
26. Ganade, C. E. et al. Tracing Neoproterozoic subduction in the Borborema Province (NE Brazil): clues from U–Pb geochronology and Sr–Nd–Hf–O isotopes on granitoids and migmatites. *Lithos* **202-203**, 167–189 (2014).
27. Kalsbeek, F., Affaton, P., Ekwueme, B., Freid, R. & Thranea, K. Geochronology of granitoid and metasedimentary rocks from Togo and Benin, West Africa: comparisons with NE Brazil. *Precambrian Res.* **196**, 218–233 (2012).
28. Lanari, P. & Duesterhoeft, E. Modeling metamorphic rocks using equilibrium thermodynamics and internally consistent databases: past achievements, problems and perspectives. *J. Petrol.* **60**, 19–56 (2019).
29. Lanari, P. et al. XMapTools: a MATLAB©-based program for electron microprobe X-ray image processing and geothermobarometry. *Comput. Geosci.* **62**, 227–240 (2014).
30. Green, D. H. & Ringwood, A. E. An experimental investigation of the gabbro to eclogite transformation and its petrological applications. *Geochim. Cosmochim. Acta* **31**, 767–833 (1967).
31. Anderson, J. L. & Smith, D. R. The effects of temperature and fO2 on the Al-in-hornblende barometer. *Am. Mineral.* **80**, 549–559 (1995).
32. Holland, T. & Blundy, J. Non-ideal interactions in calcic amphiboles and their bearing on amphibole-plagioclase thermometry. *Contrib. Mineral. Petrol.* **116**, 433–447 (1994).
33. Rubatto, D. Zircon: the metamorphic mineral. *Rev. Mineral. Geochem.* **83**, 261–295 (2017).
34. Kalsbeek, F., Frei, D. & Affaton, P. Constraints on provenance, stratigraphic correlation and structural context of the Volta basin, Ghana, from detrital zircon geochronology: an Amazonian connection? *Sediment. Geol.* **212**, 86–95 (2008).
35. Ganade de Araujo, C. E. et al. U–Pb detrital zircon provenance of metasedimentary rocks from the Ceará Central and Médio Coreaú Domains, Borborema Province, NE-Brazil: tectonic implications for a long-lived Neoproterozoic active continental margin. *Precambrian Res.* **206**, 36–51 (2012).
36. Sutra, E. & Manatschal, G. How does the continental crust thin in a hyperextended rifted margin? Insights from the Iberia margin. *Geology* **40**, 139–142 (2012).
37. Kwayisi, D., Lehmann, J. & Elburg, M. The architecture of the Buem Structural Unit: Implications for the tectonic evolution of the Pan-African Dahomeyide Orogen, West Africa. *Precambrian Res.* **338**, 55–68 (2020).
38. Caby, R. Nature and evolution of Neoproterozoic ocean-continent transition: Evidence from the passive margin of the West African craton in NE Mali. *J. Afr. Earth Sci.* **91**, 1–11 (2014).
39. Ganade de Araujo, C. E. et al. Provenance of the Novo Oriente Group, southwestern Ceará Central Domain, Borborema Province (NE-Brazil): a dismembered segment of a magma-poor passive margin or a restricted rift-related basin? *Gondwana Res.* **18**, 497–513 (2010).
40. Schmidt, M. W. & Poli, S. Experimentally based water budgets for dehydrating slabs and consequences for arc magma generation. *Earth Planet. Sci. Lett.* **163**, 361–379 (1998).
41. Cooper, G. F. et al. Variable water input controls evolution of the Lesser Antilles volcanic arc. *Nature* **582**, 525–529 (2020).
42. Skelton, A., Whitmarsh, R., Arghe, F., Crill, P. & Koyi, H. Constraining the rate and extent of mantle serpentinization from seismic and petrological data: implications for chemosynthesis and tectonic processes. *Geofluids* **5**, 153–164 (2005).
43. Kempf, E. D., Hermann, J., Reusser, E., Baumgartner, L. P. & Lanari, P. The role of the antigorite + brucite to olivine reaction in subducted serpentinites (Zermatt, Switzerland). *Swiss J. Geosci.* **113**, 16 (2020).
44. Zhu, D. C, Wang, Q, Chung, S. L, Cawood, P. A. & Zhao, Z. D. *Gangdese Magmatism in Southern Tibet and India–Asia Convergence Since 120 Ma*. (Geological Society, Special Publications, 2019).
45. Donaldson, D. G., Webb, A. A. G., Menold, C. A., Kylander-Clark, A. R. C. & Hacker, B. R. Petrochronology of Himalayan ultrahigh-pressure eclogite. *Geology* **41**, 835–838 (2013).
46. Attoh, K., Dallmeyer, R. D. & Affaton, P. Chronology of nappe assembly in the Pan-African Dahomeyide orogen, West Africa: evidence from 40Ar/39Ar mineral ages. *Precambrian Res.* **82**, 153–171 (1997). 26.
47. Lanari, P. et al. Deciphering high-pressure metamorphism in collisional context using microprobe mapping methods: application to the Stak eclogitic massif (northwest Himalaya). *Geology* **41**, 111–114 (2013).
48. De Andrade, V., Vidal, O., Lewin, E., O'Brien, P. & Agard, P. Quantification of electron microprobe compositional maps of rock thin sections: an optimized method and examples. *J. Metamorph. Geol.* **24**, 655–668 (2006).
49. Lanari, P. et al. XMapTools: a MATLAB©-based program for electron microprobe X-ray image pro-cessing and geothermobarometry. *Comput. Geosci.* **62**, 227–240 (2014).
50. Mészaros, M. et al. Petrology and geochemistry of feldspathic impact-melt breccia Abar al' Uj 012, the first lunar meteorite from Saudi Arabia. *Meteor. Planet. Sci.* **51**, 1830–1848 (2016).
51. Lanari, P. & Engi, M. Local bulk composition effects on mineral assemblages. In *Petrochronology*. Reviews in Mineralogy and Geochemistry, Vol. 83 (eds. Kohn, M. J., Lanari, P. & Engi, M.) 55–102 (The Mineralogical Society of America, 2017).
52. Williams, I. S. *Application of Microanalytical Techniques to Understanding Mineralizing Processes* Vol. 7 (eds. McKibben, M. A. et al.) 1–35 (Reviews in Economic Geology, Society of Economic Geologists, 1998) (2008).
53. Black, L. P. et al. TEMORA 1: a new zircon standard for phanerozoic U-Pb geochronology. *Chem. Geol.* **200**, 155–170 (2003).
54. Stacey, J. S. & Kramer, J. D. Approximation of terrestrial lead isotope by a two-stage model. *Earth Planet. Sci. Lett.* **26**, 207–212 (1975).
55. Ludwig, K. R. *SQUID 2: A User's Manual, Rev* (Berkeley Geochronology Center, Special Publication, 2009).
56. Ludwig, K. R. *Isoplot/Ex version 3.0. A Geochronological Toolkit for Microsoft Excel* (Berkeley Geochronological Centre, Special Publication, 2003).
57. Eggins, S. M., Kinsley, L. P. J. & Shelley, J. M. G. Deposition and element fractionation processes during atmospheric pressure laser sampling for analysis by ICP-MS. *Appl. Surf. Sci.* **129**, 278–286 (1998).
58. Jochum, K. P. et al. Determination of reference values for NIST SRM 610–617 glasses following ISO guidelines. *Geostand. Geoanal. Res.* **35**, 397–429 (2011).
59. Sun, S. S. & McDonough, W. F. In *Magmatism in Ocean Basins* Vol. 42 (eds. Saunders, A. D. & Norry, M. J.) 313–345 (Geological Society of America Special Paper, 1989).

60. de Capitani, C. & Brown, T. H. The computation of chemical equilibrium in complex systems containing nonideal solutions. *Geochim. Cosmochim. Acta* **51**, 2639–2652 (1987).
61. Holland, T. J. B. & Powell, R. An internally consistent thermodynamic data set for phases of petrological interest. *J. Metamorph. Geol.* **16**, 309–343 (1998).
62. White, R. W., Powell, R. & Holland, T. J. B. Progress relating to calculation of partial melting equilibria formetapelites. *J. Metamorph. Geol.* **25**, 511–527 (2007).
63. White, R. W., Powell, R. & Clarke, G. L. The interpretation of reaction textures in Fe-rich metapelitic granulites of the Musgrave Block, central Australia: constraints from mineral equilibria calculations in the system K_2O–FeO–MgO–Al_2O_3–SiO_2–H_2O–TiO_2–Fe_2O_3. *J. Metamorph. Geol.* **20**, 41–55 (2002).
64. Diener, J. F. A., Powell, R., White, R. W. & Holland, T. J. B. A new thermodynamic model for clino- and orthoamphiboles in the system Na_2O-CaO-FeO-MgO-Al_2O_3-SiO_2-H_2O-O. *J. Metamorph. Geol.* **25**, 631–656 (2007).
65. Green, E. C. R., Holland, T. J. B. & Powell, R. An order-disorder model for omphacitic pyroxenes in the system jadeite-diopside-hedenbergite-acmite, with applications to eclogite rocks. *Am. Mineral.* **92**, 1181–1189 (2007).
66. Baldwin, J. A., Powell, R., Brown, M., Moraes, R. & Fuck, R. Modelling of mineral equilibria in ultrahigh-temperature metamorphic rocks from the Anápolis-Itauçu Complex, central Brazil. *J. Metamorph. Geol.* **23**, 511–531 (2005).
67. Holland, T. J. B. & Powell, R. An improved and extended internally consistent thermodynamic dataset for phases of petrological interest, involving a new equation of state for solids. *J. Metamorph. Geol.* **29**, 333–383 (2011).
68. Green, E. C. R. et al. Activity-composition relations for the calculation of partial melting equilibria for metabasic rocks. *J. Metamorph. Geol.* **34**, 845–869 (2016).
69. Lanari, P., Giuntoli, F., Loury, C., Burn, M. & Engi, M. An inverse modeling approach to obtain P-T conditions of metamorphic stages involving garnet growth and resorption. *Eur. J. Mineral.* **29**, 181–199 (2017).
70. Tairou, M. S. & Affaton, P. Structural organization and tectono-metamorphic evolution of the Pan-African suture zone: case of the Kabye and Kpaza massifs in the Dahomeyide orogen in Northern Togo (West Africa). *Int. J. Geosci.* **4**, 166–182 (2013).

Acknowledgements

This research was supported by the Serrapilheira Institute (grant # Serra—1709-21887), Swiss National Science Foundation project N IZESO_l94628 and by the Geological Survey of Brazil. C.E.G. acknowledges the CAPES Higher Education Improvement Coordination 88881.363575/2019-01 for supporting the author's research visit at the University of Bern. C.E.G and C.M.R thank Julio Cezar Mendes for the help in the EPMA data of sample DKE-380.

Author contributions

C.E.G, P.L., D.R., J.H., and R.F.W. equally contributed in project conceptualization, idea refinement and writing. C.E.G., M.A.S.B., R.C., and Y.A. collected the samples and field data. C.E.G. and D.R. acquired U-Pb ages and zircon trace elements. P.L., C.E.G., and L.R.T. acquired EPMA data and performed the thermodynamic modeling. C.M.R. acquired EPMA data for sample DKE-380.

Competing interests

The authors declare no competing interests.

Additional information

Supplementary information The online version contains supplementary material available at https://doi.org/10.1038/s43247-021-00103-z.

Correspondence and requests for materials should be addressed to C.E.G.

Peer review information Primary handling editor: Joe Aslin.

Reprints and permission information is available at http://www.nature.com/reprints

Publisher's note Springer Nature remains neutral with regard to jurisdictional claims in published maps and institutional affiliations.